Impedance-based Rapid Diagnostic Tool for Single Malaria Parasite Detection

Marco Giacometti, Tommaso Pravettoni, Jonathan Barsotti, Francesca Milesi, Cainã de Oliveira Figares, Federico Maspero, Lorenzo P. Coppadoro, Giovanni Benevento, Mariagrazia Ciardo, Pietro Alano, Gianfranco B. Fiore, Riccardo Bertacco, and Giorgio Ferrari *Member, IEEE*

***Abstract*— This paper presents a custom, low-cost electronic system specifically designed for rapid and quantitative detection of the malaria parasite in a blood sample. The system exploits the paramagnetic properties of malaria-infected red blood cells (iRBCs) for their magnetophoretic capture on the surface of a silicon chip. A lattice of nickel magnetic micro-concentrators embedded in a silicon substrate concentrates the iRBCs above coplanar gold microelectrodes separated by 3 µm for their detection through an impedance measurement. The sensor is designed for a differential operation to remove the large contribution given by the blood sample. The electronic readout automatically balances the sensor before each experiment and reaches a resolution of 15 ppm in the impedance measurement at 1 MHz allowing a limit of detection of 40 parasite/µl with a capture time of 10 minutes. For better reliability of the results, four sensors are acquired during the same experiment. We demonstrate that the realized platform can also detect a single infected cell in real experimental conditions, measuring human blood infected by *Plasmodium falciparum* malaria specie.**

Keywords*— *malaria, plasmodium, hemozoin, lab-on-a-chip, biosensor, health, diagnostic, impedance detection, magnetophoresis, lock-in amplifier.

I. Introduction

According to the World Health Organization (WHO), malaria has affected 241 million people in 2020, causing more than 627000 deaths [1]. Malaria is a parasitic disease caused in humans by five species of *Plasmodium* parasite. If not promptly diagnosed and treated, it may lead to severe forms of malaria, which are potentially fatal, particularly in the case of *P. falciparum*.

Plasmodium is transmitted to humans through the bite of infected Anopheles mosquitoes, the malaria parasite vector. Once in the body, the parasites infect the red blood cells (RBCs). During the intraerythrocytic stage, the *plasmodium* consumes the hemoglobin of the host cell, converting it into insoluble crystals of β-hematin, also called hemozoin crystals (HCs) or malaria pigment [2]–[4]. These crystals have paramagnetic properties, making them and the red blood cells containing them attracted by a magnet [5]–[7].

Despite the availability of disease treatments and the intense efforts put in place to eradicate the disease agent, a prompt diagnosis in endemic zones during the early stages of the illness is still required [1]. In addition to a low price and high sensitivity, a suitable malaria diagnostic tool for endemic zones should be fast, user-independent, and digital in order to collect data to track the disease evolution in different areas.

Unfortunately, currently available techniques struggle to successfully combine all these features [6, 8, 9]. Techniques based on the polymerase chain reaction (PCR) are highly sensitive (< 1 parasite/µl) and able to distinguish among different malaria species. Nevertheless, each test is expensive and time-consuming (about one hour). In addition, it is hardly compatible with on-field applications due to the technical requirements of equipment and sample preparation [10]. Optical microscopy is still the reference diagnostic technique for malaria, especially for on-field applications. At its best, it combines a good sensitivity (c.a. 40 parasite/µl) with moderate equipment costs. However, it requires a skilled operator fully occupied for about one hour for each test. In addition, the optical blood smear test result is intrinsically strongly dependent on the operator's capabilities and interpretation [9]. As a result, the quality of the diagnosis is typically worse than the best achievable performance, resulting again in additional costs for the medical system. Finally, antigenic rapid diagnostic tests (RDTs) are primarily adopted for their very convenient price and fast execution (15-20 mins) compared to the other techniques. Despite being the most largely used diagnostic test in on-field applications, RDTs performance in endemic zones is limited and threatened by the diffusion of parasites without the genes *pfhrp2* and *pfhrp3* [11], [12], encoding the target antigens of the RDTs. Consequently, there is an increasing number of false negatives [8], [13].

Recently, many techniques were proposed to solve the limitations of the currently used diagnostic tools [14-25]. However, these systems usually require complicated sample preparation or complex microfluidic apparatus that prevents on field-application. Promising point-of-care devices are based on hemozoin detection [26], using optical detection [25] or exploiting magnetic properties of the HCs for a magneto-optic [20, 21] or inductive [24] measurement. Their main limitation is the need to extract the HCs from the infected cells, preventing a quantification of the parasitemia, i.e., the percentage of infected red blood cells (iRBCs). Direct detection of the iRBC in whole blood was demonstrated using a photoacoustic-surface acoustic wave sensor [22, 23]. However, the sensitivity is still poor (>10'000 parasite/µl), and a low-cost operation is not demonstrated yet.

In previous work, we proposed TMek, an innovative diagnostic tool based on the paramagnetic properties of HCs

Manuscript received June 1, 2022. This work was supported by Politecnico di Milano under the Polisocial Awards 2016 and Switch2Product 2018 Awards.

M. Giacometti, T. Pravettoni, J. Barsotti. F. Milesi, C. Figares, L. P. Coppadoro, G. Benevento, and G.B. Fiore are with Dipartimento di Elettronica, Informazione e Bioingegneria, Politecnico di Milano, Milano, 20133 Italy.

M. Ciardo and P. Alano are with Dipartimento di Malattie Infettive, Istituto Superiore di Sanità, Roma 00161, Italy.

F. Maspero, R. Bertacco and G. Ferrari are with Dipartimento di Fisica, Politecnico di Milano, Milano, 20133 Italy (*giorgio.ferrari@polimi.it*).

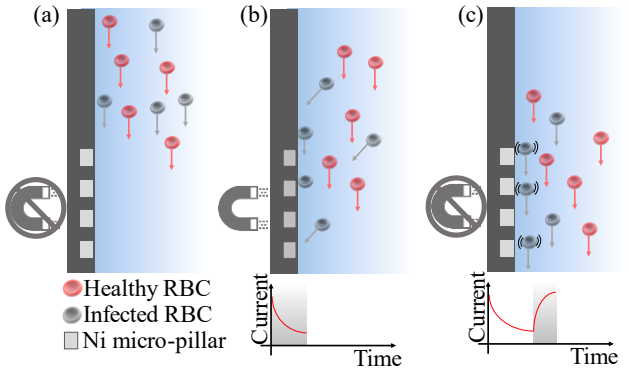

Figure 1 - Schematics of the working principle of the proposed diagnostic platform. The silicon chip is in vertical position and the RBCs are free to sediment (a). A permanent magnet attracts the iRBCs, and the magnetic concentrator captures them (b) allowing an impedimetric detection. The removal of the permanent magnet releases the iRBCs (c).

in iRBCs [27, 28]. TMek uses the competition between gravity and magnetic forces to separate infected cells from healthy ones. TMek quantifies the infection by an impedimetric measurement which senses the current variation induced by iRBCs magnetically captured at the electrode/blood-sample interface.

In this work, we present a low-cost yet sensitive electronic platform for an effective and compact implementation of the TMek diagnostic tool disclosed and validated in [27]. It implements a lock-in amplifier for low-noise impedance measurement of the differential sensor in the MHz range. A microcontroller allows the auto-balancing of the differential sensors, the setting of the measurement parameters, and data acquisition. The platform, successfully used for the on-field campaign in Cameroon presented in [27], is described here for the first time. Moreover, thanks to a careful analysis of the platform noise limit, a new sensor layout was designed and used to show the possibility of achieving the remarkable result of single-cell sensitivity on malaria parasite-infected human blood samples. The rest of the paper is organized as follows: in section II, we describe TMek working principle, the digital rapid diagnostic test for malaria the board has been developed for, emphasizing the requirements for the sensor readout. Section III treats materials and methods focusing on the different system components, in particular the chip sensor and the electronic board. In Section IV, we present the performance of the electronic platform and its application in detecting infected RBCs in human blood samples.

II. Working Principle

The magnetophoretic force, F_m, acting on a magnetic particle depends on the difference between the magnetic susceptibility of the particle and the surrounding medium, $\Delta\chi$, the volume of the particle, V_p, and the gradient of the magnetic field squared, ∇H^2, according to:

$$F_m = \frac{1}{2}\mu_0 V_p \Delta\chi \nabla H^2 \tag{1}$$

where μ_0 is the vacuum permeability. The magnetophoretic force is used to capture the iRBCs with the configuration shown in Fig. 1. The blood sample is put between a glass slide and a silicon chip placed in a vertical position, with the gravity vector parallel to its surface. A spacer on the glass slide surface defines the thickness of the blood smear, thus the maximum distance of the RBCs from the chip surface. In this configuration, healthy RBCs settle under the action of the gravity force. A permanent magnet is put in close contact with the back of the chip, producing a magnetic field gradient high enough ($|\nabla H^2| > 10^{14}\,\frac{A^2}{m^3}$) [27] to attract iRBCs on the chip surface. The blood drop is diluted six times in PBS to reduce its RBC density in order to inhibit the motion competition between healthy red blood cells (hRBCs) and iRBCs. In order to concentrate the iRBCs in specific sensing areas and facilitate their electrical detection, we embedded Ni micro-pillars in the silicon chip. When immersed in the magnetic field of the permanent magnet, these structures become magnetized, acting as localized magnetic field concentrators. Thus, the pillars bend the trajectory of the iRBCs, attracting them close to the sensing sites, while the healthy ones are not (Fig. 1b). Once captured and concentrated near the Ni micro-pillars, the iRBCs can be detected and quantified by measuring the impedance between two microelectrodes fabricated on the chip surface and positioned above the Ni pillars.

The cellular membrane makes a RBC an insulating object for frequencies below 10 MHz with a conductivity σ_p much smaller than the conductivity σ_m of the surrounding medium, the blood plasma [29]. The conductivity of the medium containing particles, σ_{mix}, can be obtained from Maxwell's mixture theory [30]:

$$\sigma_{mix} = \sigma_m \frac{1+2\phi\left(\frac{\sigma_p-\sigma_m}{\sigma_p+2\sigma_m}\right)}{1-\phi\left(\frac{\sigma_p-\sigma_m}{\sigma_p+2\sigma_m}\right)} \tag{2}$$

where ϕ is the volume fraction occupied by the RBCs in the detection region, proportional to the number and volume of infected cells.

In the case of insulating particles ($\sigma_p \approx 0$), as the RBCs, occupying a small volume fraction ($\phi \ll 1$), Eq. (2) can be simplified as:

$$\sigma_{mix} = \sigma_m \left(1 - \frac{3}{2}\phi\right) \tag{3}$$

The relative conductance variation, $\Delta G/G_0$, caused by the captured iRBCs inside the detection volume of interest can be obtained by:

$$\frac{\Delta G}{G_0} = \frac{G_{mix}-G_0}{G_0} = -\frac{3}{2}\phi \tag{4}$$

where G_{mix} and G_0 are, respectively, the medium conductance with and without particles. Thus, the number and volume of iRBCs captured near the electrodes are correlated to the measurement of the medium conductivity. The conductance is extracted by an impedance measurement at a sufficiently high frequency (≥1 MHz in our case) to shunt the double-layer capacitance at the electrode-liquid interface and low enough (<10 MHz) to neglect the membrane

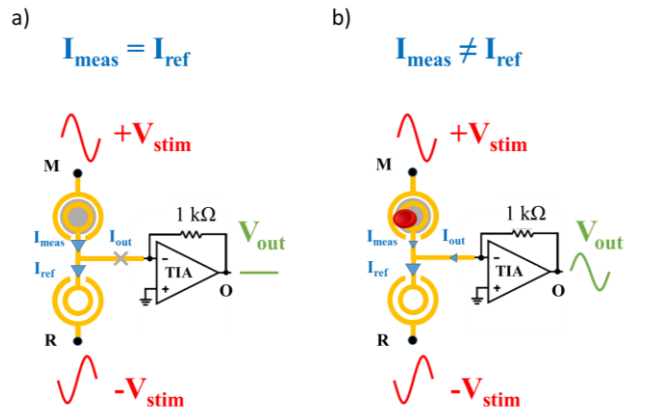

Figure 2 - Schematics of the differential technique showing applied bias (red), the output signal (green), and the currents values (blue). When no corpuscles are captured, measure (M) and reference (R) electrodes currents, I_{meas} and I_{ref}, respectively, are equals and opposite in sign, eliciting at the amplifier input, where total I is null. On the contrary, when a corpuscle is captured at M in presence of the magnetic field, I_{meas} decreases making the I_{meas} - I_{ref} different from zero.

capacitance of the cells obtaining a more accurate measure of the cell volume.

After the capture of the infected cells, the permanent magnet is withdrawn, releasing the captured iRBCs. The current returns to its initial value as the cells move away from the electrodes due to Brownian motion and gravity force (Fig. 1c). The relatively fast release of cells (less than one minute in our setup) makes this current variation a more reliable quantification of the captured cells because it is less affected by drift than the slower capture phase (10 minutes in a typical experiment).

A. *Differential impedance measurement*

The sensor impedance is measured with the differential scheme shown in Fig. 2. A sinusoidal voltage with an amplitude of 100 mV and a frequency of 1 MHz is applied to the measurement electrodes. A counter-phase sinusoidal voltage is applied to the reference electrodes, having the same geometry as the measurement electrodes. The reference electrodes do not have Ni micro-pillars for concentrating the magnetic field, thus preventing the local concentration of the iRBCs. The currents that flow in the measure and reference electrodes are collected by a single electrode, as shown in Fig. 2. Given the counter-phase voltages applied to the electrodes, only the current difference is amplified by the transimpedance amplifier. In Fig. 2a, we show the schematic of the differential measures when no cells are captured at the Measure electrode surface (magnetic field OFF), and, ideally, the currents are equal ($I_{meas} = I_{ref}$), resulting in a constant 0 V output after the TIA. When an iRBC is captured (magnetic field ON), the local conductivity varies, modifying only the I_{meas}. Consequently, the current becomes different, producing a non-zero output (Fig. 2b). The current difference measured in the MHz range, where the double-layer capacitance can be neglected, is:

$$\Delta I = \Delta G \cdot V_{stim} \qquad (5)$$

where V_{stim} is the amplitude of the AC voltage applied to the electrodes and ΔG is the conductance variation given by Eq. (4). With this technique, we convert the number of captured particles (i.e., the volume fraction) into the current ΔI, which is the raw signal obtained from the electronic instrument.

The differential scheme removes the current contribution given by the conductivity of the blood sample, G_0 in Eq. (4), which is orders of magnitude larger than the useful signal ΔI. This not only relaxes the dynamic range requirements of the electronic readout but also reduces the sensitivity of the measurement to fluctuations of the blood conductivity given, for example, by a change of temperature or of the ionic concentration. Moreover, high-resolution measurements based on lock-in amplifiers may be limited by the random variations of the gain along the acquisition chain [31, 32]. By adopting the differential scheme of the sensor, the gain fluctuations produce a spurious noise proportional to the current ΔI and not to the much larger current $G_0 V_{stim}$.

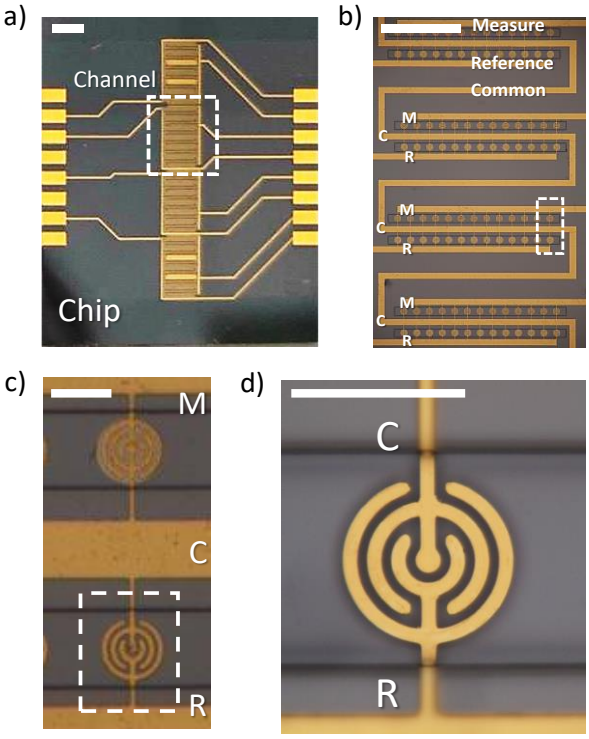

Figure 3 - Photograph of the full silicon chip composed by 4 independent channels (a). The measure (M) and reference (R) electrodes are alternated with a common (C) connection (b). The microscope images in (c) and (d) show a couple of measure and reference microelectrodes and a zoom of a single electrode layout, respectively. Scale bars: 1 mm (a), 500 µm (b), 40 µm (c) and (d).

III. Materials and Methods

A. *Chip design and fabrication*

An optical image of the whole chip is reported in Fig. 3a. It contains four independent sensors of 1 mm x 3.8 mm allowing four parallel measurements on the same blood sample, improving the reliability of the final result. Each sensor presents, buried into the Si substrate, the Ni cylindrical micro-concentrators to selectively concentrate infected RBCs on measurement electrodes [27, 33]. The shape and geometrical parameters of the magnetic micro-concentrators have been determined using FEM simulations [33]. The chip used in our previous works has the micro-concentrators uniformly distributed on the surface with a hexagonal lattice

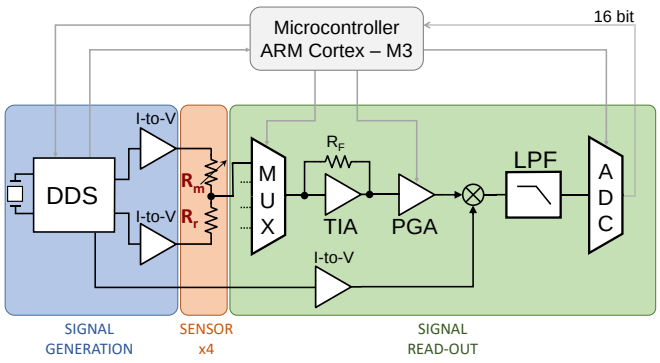

Figure 4 – Simplified schematics of the electronic board. The signal generator stage (blue) provides in-phase and counter-phase AC signals applied to the sensor (chip, orange). The output current from each sensor is passed to the amplification stage (green) through an analog multiplexer, then amplified (PGA), demodulated, filtered, and finally converted in a digital output by an ADC.

arrangement. Here, the layout was optimized to reduce the number of electrodes (from 350 to 91), maintaining a similar detection limit. This was achieved by arranging the micro-concentrators in 7 rows, equally spaced by 600 µm, each having a diameter of 40 µm, 20 µm height, and center-center spaced 80 µm each other. The external magnetic field attracts the iRBCs on the chip surface, and the gravity moves them down until they are captured by the local high magnetic force generated by the Ni pillars. The 80 µm separation of the pillars on a row prevents an iRBC from passing through without being captured. The vertical separation of the rows is a trade-off between the number of pillars and the capture phase duration. Few rows largely separated concentrate the captured iRBCs on a limited number of electrodes facilitating the electrical detection. On the other side, the iRBCs have to cover a longer distance before being captured, making the measurement longer. A row spacing of 600 µm was experimentally determined to retain approximately the same capability in capturing the iRBCs in 10 minutes of the old chip layout but using less than one-third of micro-concentrators.

The micro-concentrators are fabricated on a heavily p-doped Si-substrate (P+/Boron, 0.005-0.025 Ω·cm). The shape of the pillars is defined by optical lithography on a 20 µm positive resist (AZ® 40 XT, Microchemicals), leaving circular areas of the Si-substrate uncovered. The photoresist is then used as a mask for the etching of the cylindrical holes by reactive ion etching. Subsequently, a 20 nm seed layer of Ni is deposited on the substrate via e-beam evaporation. The photoresist lift-off leaves the seed layer only on the bottom of the cavities. The holes are then filled with Ni by electroplating in a Ni-sulfamate solution (Tecnochimica S.p.a.), using the heavily doped substrate itself as electric contact, ensuring the electrical connection between the seed layers with the power supply (Silicon Wafer Plating Laboratory Set YTC300, Yamamoto-MS Co.). At last, the substrate is planarized through mechanical polishing to get rid of the uneven filling of the cavities.

The electrodes for the impedimetric detection of iRBCs are deposited on a 3 µm layer of SiO_2 grown on the chip surface after the fabrication of the magnetic concentrators. The significant thickness of the silicon oxide reduces the parasitic capacitances between the electrodes and the silicon substrate, with a beneficial effect on the noise produced by the front-end electronics. Each sensor comprises two electrode sets: the Measure above the magnetic concentrators and the Reference without concentrators required for the differential readout. Measure and Reference rows are alternated (see the zoom in Fig. 3b) for better differential measurements. Since the magnetic concentrators capture the iRBCs in random positions, the electrodes are circular and cover all the surfaces above the Ni micro-pillar, as shown in Fig. 3c and 3d. All the 91 pairs of differential electrodes are connected in parallel. The electrodes are fabricated with 200 nm of gold, using 30 nm of Cr as an adhesion layer. The gap between the electrodes and their width is 3 µm, compatible with standard optical lithography. Based on FEM simulations, these values confine the electric field in a volume similar to that occupied by a single RBC, providing a significant impedance change for each captured cell (Eq. 4). A smaller geometry requires a more complex fabrication process without a significant improvement of the electrical signal.

Compared to the old chip layout, the reduced number of electrodes and the interleaving of Measure and Reference areas of the new layout have contributed to reducing the number of invalid measurements from about 20% down to about 2%.

B. Electronic Design

A custom board implementing a Lock-in Amplifier has been designed for a low-noise reading of the signals from the four sensors. A schematic diagram of the electronic board is reported in Fig. 4. Each sensor can be modeled as two resistors of R ≈ 100 Ω, corresponding to the Measure and Reference areas, with a common terminal kept to 0 V by a transimpedance amplifier (TIA). Two counter-phase sinusoidal voltage signals drive the two external nodes of the resistors, and the current flowing in the common terminal is converted into a voltage by the TIA. Any unbalance given by the capture of the iRBCs on the Measure resistor is amplified and demodulated by an analog lock-in detector. The 1 MHz sinusoidal signals are generated using a four-channel single-chip DDS component (AD9106). This solution was preferred over the use of fast DACs controlled by the digital processor

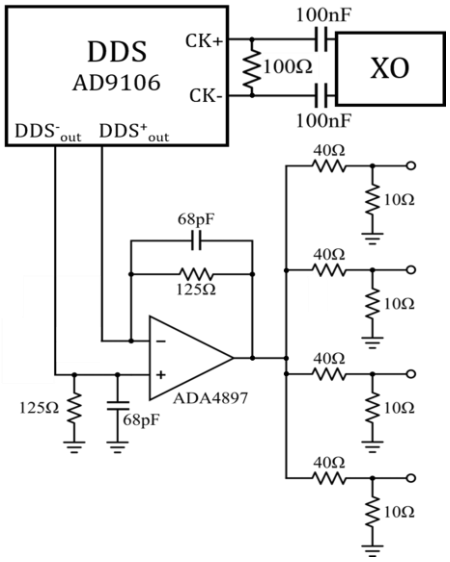

Figure 5 – Schematic of the signal generation block.

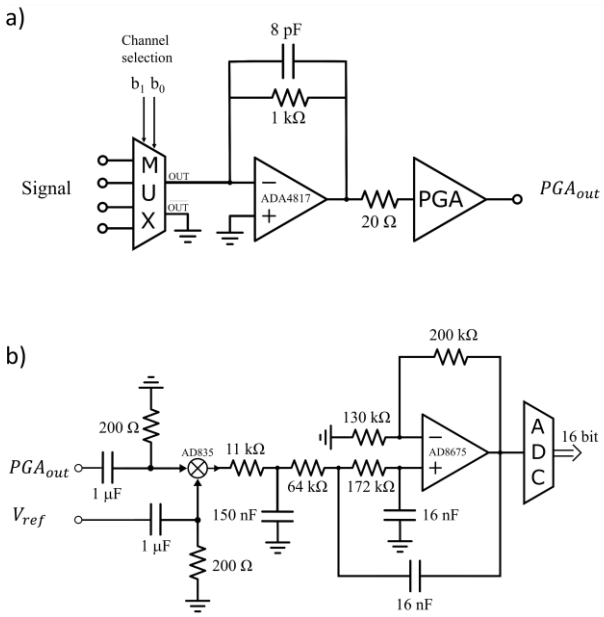

Figure 6 - Schematics of the signal read-out with the amplification stage (a) and the lock-in stage (b).

to utilize a low-cost microcontroller. The DDS can generate four analog sinusoids with the same frequency but different and digitally programmable phases and amplitudes. The 12-bit amplitude modulation feature of the component was exploited to compensate for the fabrication tolerances of the electrodes and of the components along the generation path that unbalance the differential resistive structure. The amplitudes of the two counter-phase signals are automatically tuned before starting a measurement in order to have an approximately null current read by the TIA. The clock source of the DDS is an external 80 MHz crystal oscillator (540BAA80M00BAG by Skyworks) connected to it through the LVDS standard, as shown in Fig. 5. The differential current signals coming from the DDS component are converted to a single-ended voltage with a conversion factor of 125 Ω by an amplifier with a closed-loop bandwidth of 20 MHz. A passive voltage divider reduces the voltage applied to the sensor by a factor of 5 and correspondently decreases the output noise down to $0.35\ nV/\sqrt{Hz}$. The final signal amplitude applied to the sensor is about 100 mV, which is low enough to avoid red-ox reactions at the electrode surface. As shown in Fig. 5, each sensor has an independent voltage divider to avoid that a short-circuited faulty sensor hampers any measurement.

The common nodes of the four sensors are connected to a low-on resistance multiplexer made by four single-pole double-throw analog switches (MAX4622), which connect the sensors in sequence to a single transimpedance amplifier (ADA4897). Differently from a standard analog multiplexer, the unselected sensors are kept to ground ($\overline{OUT}$ in Fig. 6a), that is, the same potential of the input node of the TIA. Thus, the sensors are always biased with about the same voltage minimizing the current transient due to the electrode-electrolyte interface when selected. As reported in Fig. 6a, the TIA is based on the low-noise wide-bandwidth operational amplifier ADA4817. The sizing of the feedback resistor, R_F = 1 kΩ, and feedback capacitor, C_F = 8 pF, have been chosen to guarantee low noise (thermal noise of R_F about ten times lower than the sensor's noise), a bandwidth wider than 10 MHz, and the feedback stability for input capacitance of hundreds of pF (about 100 pF given by the sensor and ≈ 250 pF of the analog multiplexer).

The output of the TIA is then amplified by a voltage amplifier (G = 5) and a programmable gain amplifier (G = 0.08-10), both implemented using the component THS7001. In order to avoid fast analog-to-digital converters and powerful digital processors, the lock-in operation at 1 MHz is implemented in the analog domain. As shown in Fig. 6b, the PGA output signal is multiplied using an analog multiplier (AD835) with a reference sinusoidal signal V_{ref} at the same frequency as the stimulus signal implementing a single-phase lock-in amplifier. All the sinusoidal signals are generated by the DDS component with a programmable phase starting from the same master clock, assuring no internal phase drift. The reference phase is calibrated to compensate for the phase shifts added by the analog circuits and extract the real part of the sensor admittance at 1 MHz. In order to improve the analog multiplication accuracy, the PGA output and the reference signal are high-pass filtered to remove the DC value with a passive CR filter whose pole is set to 800 Hz. A third input of the analog multiplier (not shown in Fig. 6b) is used to sum a constant voltage to the multiplication outcome obtaining an output voltage between 0 V and 2 V. The resulting signal is then low pass filtered at 100 Hz with a cascade of a 1-pole RC filter and a 2-poles Sallen Key active cell, implementing a Chebyshev filter used as an antialiasing filter. Finally, the signal is sampled at 10 kS/s by a low-power 16-bit ADC (AD7680).

A microcontroller ARM Cortex-M3 (Atmel SAM3X8E) is used to configure the DDS and the PGA and manage the measurement. Before starting a measurement, the AC voltage stimuli required for balancing the differential structure are automatically determined for each sensor independently. During the measurement, the microcontroller scans the four sensors with a frequency of 4 Hz. At each switching of the input sensor, the DDS is set with the proper amplitude gains to read the selected sensor in a balanced condition. The analog-to-digital conversion is started after 50 ms from the commutation of the sensor to avoid the transient mainly given by the low-pass filter. For each sensor, 2000 samples are acquired at 10 kS/s. The samples are averaged to reduce the noise added by the ADC and the equivalent noise bandwidth. Every second, the four samples resulting from the admittance measurement of the sensors are sent to a PC via USB communication. The microcontroller is also used to automatically detect the connection and disconnection of the silicon chip with the electrodes.

The entire board has a size of 12 cm x 10 cm and is powered from a ±12 V dual supply, and the current consumption is 150 mA. A custom software developed in MATLAB using App Designer allows to set the measurement parameters, start/interrupt the experiment, control the movement of the permanent magnet, and visualize in real-time the test output.

C. Experimental setup

The diagnostic platform consists of two main components: a cartridge for the disposable silicon chip (Fig. 7a) and an

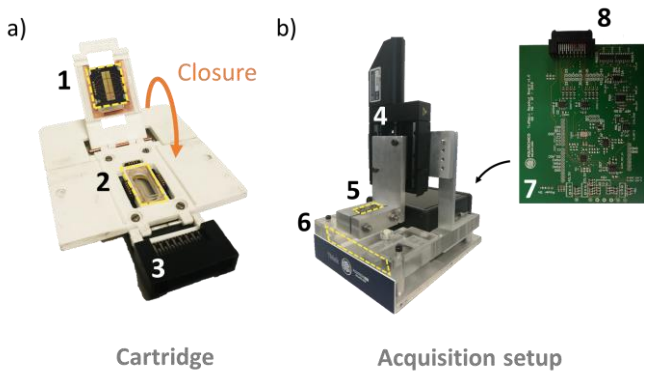

Figure 7 - Picture (a) shows the cartridge with the chip slot containing the chip (1), the gasket (2), and the PCB connector (3). The arrow shows the closure movement to couple and seal the gasket and the chip. Picture (b) shows the motor (4) that controls the permanent magnet (5) position and the cartridge slot (6) where the cartridge is inserted and coupled with the PCB board (7) through the connector (8).

acquisition setup (Fig 7b). The former, manufactured by 3D printing, has two housing for the chip placement and a glass slide with a gasket on which the blood sample is placed. The cartridge can be closed by a pivot, putting the chip into contact with the gasket, thus defining a close chamber containing the sample. The chamber size is about 8 mm x 15 mm x 550 µm for a total blood volume of 70 µl. Two rows of spring contacts (Mill-Max 854-22-006-10) mounted on a PCB placed beneath the 3D printed cartridge make electrical contact with the pads of the chip. The PCB transfer the chip signals to a board-to-board connector (TX25-30P-LT-H1E by JAE Electronics) soldered on it, whose complementary socket (TX24-30R-LT-H1E) is mounted on the electronic board. The cartridge PCB is made of four layers; the two inner layers contain the signal tracks from and to the chip, while the two external layers are ground planes to shield the formers from electromagnetic interferences. The cartridge presents a hole beneath the chip to allow the permanent magnets to approach the chip backplane.

The mechanical setup (Fig. 7b) presents a lodging for the cartridge insertion and connection with the electronic board positioned on the rear of the setup. A stepper motor (L406-20SD00L by PI), attached to the structure, allows the movement of two permanent magnets to and from the back of the chip. In order to maximize the magnetic field generated by the permanent magnet, and its gradient, a magnet assembly has been exploited. Two 20 mm x 20 mm x 5 mm parallelepiped shaped N42 grade NdFeB permanent magnets by K&J Magnetics Inc, have been put in contact, on their largest face, by a press-like custom mechanical apparatus. The two faces have opposite magnetization directions and thus are strongly repelled to each other. A µ-metal sheet (200 µm thickness) is put between the two to allow a stable mechanical assembly as well as to convey and concentrate the magnetic field lines of the permanent magnets. In this way, a strong magnetic field gradient is produced, corresponding to a $|\nabla H^2| > 10^{14} \frac{A^2}{m^3}$. Close to Ni concentrators, instead, the gradient of H^2 is one order of magnitude higher, thus focusing the iRBCs on the electrodes placed above the Ni concentrators.

D. *P. falciparum infected RBC preparation*

The *P. falciparum* line NF54 was cultivated by standard methods to produce the iRBC used in this work. In order to obtain purified gametocyte-iRBCs, a culture of asexual blood stages grown in human 0^+ RBCs was induced to produce synchronous gametocytes by growth at high (10-12%) parasitemia, followed by a 48 h treatment with 50 mg/ml N-Acetyl Glucosamine to clear residual asexual stage parasites. At day 10 of maturation, gametocyte-iRBCs were purified from uninfected RBCs through MACs Separation Columns CS (Miltenyi Biotec) and resuspended in PBS, as described in [27]. To obtain purified 18 (±2) h late ring stage parasites, mature asexual schizonts were enriched by sedimentation on a 60% Percoll cushion and were incubated with uninfected RBCs to allow schizonts to burst and the progeny of merozoites to infect RBCs. After 4 h, this culture was treated with 5% sorbitol to clear residual schizonts [34], producing a culture with 23% of the RBCs infected by synchronous (4h time window) ring stage parasites. After additional 14 h, this culture was centrifuged and resuspended in PBS to perform the measurements on the 18 (±2) h late ring-iRBCs.

IV. Results

A. *Electrical characterization*

The electronic board has been fully characterized and compared with the expected performances.

We measured the transfer function from the TIA input to the multiplier one for different PGA gains (1.26, 2.52, 5.01, 10 V/V) using an E5061B Network Analyzer by Agilent Technologies. A 60 Ω resistor was used to mimic the minimum resistance of one sensor area and inject a current into the TIA input. Fig. 8a shows the result of the transfer function measurement. The high pass filter effect dominates at frequencies below 800 Hz, which is the HPF pole. At higher frequencies, the transfer function shows a plateau whose amplitude is given by the cascade of the TIA (1 kV/A), preamplifier (5 V/V), and PGA gains. As expected, the pole around 10 MHz introduced by the TIA limits the bandwidth of the measurement chain.

Given the application, an important parameter to consider is the noise introduced by the electronics. Its value should be lower than the noise contribution given by the sensor, which is at least the thermal noise of the measure and reference resistances connected at the virtual ground of the TIA. The noise performances of the same circuit part have been assessed by measuring its noise power spectral density utilizing a N9020A MXA Signal Analyzer by Agilent Technologies. A 30 Ω resistor, mimicking the parallel between the Measure and Reference areas resistances, has been added at the TIA input. Fig. 8b reports the noise power spectral densities measured at PGA output, setting its gain to 10 V/V (yellow line) and 1.26 V/V (black line). The white noise levels around the stimulus signal frequency (1 MHz) are approximately 1.6 µV/√Hz and 0.2 µV/√Hz for 10 and 1.26 PGA gains, respectively. Noteworthy, we observe that such noise levels are mainly dominated by the unavoidable thermal noise given by the sensor equivalent resistance, whose contribution is 1.2 µV/√Hz and 0.14 µV/√Hz for the two selected PGA gains. Thus, we can conclude that the noise

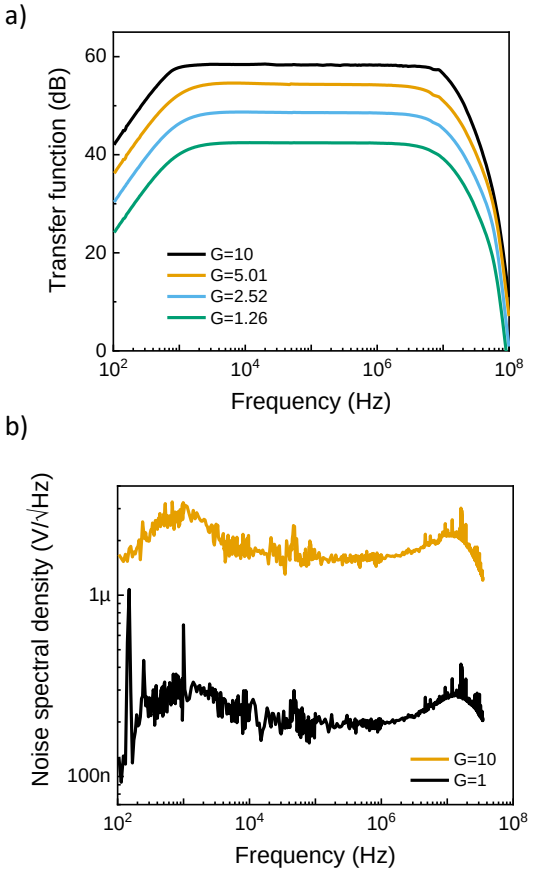

Figure 8 - Transfer function of the acquisition chain (TIA, Preamplifier, PGA and HPF) at different PGA gains (a). Voltage noise spectral density of the acquisition chain at 10 V/V (yellow line) and 1.26 V/V (black line) PGA gain (b).

introduced by the front-end electronics is negligible compared to that of the sensor.

Based on these results, the expected noise of the AC current measured at 1 MHz with the onboard lock-in amplifier should be about 150 pA rms with a bandwidth of 10 Hz. However, when performing the impedance measurements by applying an AC voltage of 100 mV on physical resistors of 150 Ω emulating the sensor, we recorded a noise of about 4 nA rms, limiting the resolution of the impedance measurement to 6 parts per million (ppm). We ascribed the additional noise to small random fluctuations of the AC voltages generated by the DDS. Random amplitude modulations of the sinusoidal voltages applied to the resistors produce a noisy AC current that is down-converted by the analog multiplier producing additional noise at the output of the system, similarly to the discussion in [31]. In agreement with this explanation of the additional noise, by decreasing the amplitude of the AC voltages and correspondingly the additional noise given by the random amplitude modulation, we reached a condition limited by the thermal noise of the resistors and the front-end electronics.

Finally, the impedance measurements with the PBS sample have shown a current noise of about 14 nA, a factor 3.5 times higher than the value recorded with physical resistors of the same value of the sensor. We hypothesize that the additional noise is given by the fluctuations in the conductivity of the ionic solution due to inhomogeneous temperature changes in the Measure and Reference areas of the sensor. A physiological solution like phosphate buffer solution, which has the same ionic composition as the blood plasma, shows a conductivity change $\Delta\sigma/\sigma$ against a variation of 1°C of approximately 1.5 % [35]. Consequently, a temperature fluctuation of 1 mK is sufficient to produce a current variation of 15 nA flowing in the ≈ 100 Ω resistance when 100 mV is applied. Since the current fluctuations given by the generated AC voltages and the temperature variations are proportional to the conductance of the sensor, a way to reduce their effect is by increasing the resistance value, as will be shown in Sec. IV-C.

Note that the low noise level reached in the actual condition of the experiments allows the detection of a variation as small as 15 ppm of the sensor impedance, a value better than bulky and expensive commercial lock-in amplifiers operating at the same frequency [31, 32].

B. Measurements of RBCs

After the electrical characterization, we evaluated our platform on biological samples to verify its capability to detect infected cells. We started measuring samples of bovine red blood cells treated with $NaNO_2$ (tRBCs), following the protocol described in [5], in order to assess both the quantification and the limit of detection (LoD) of the system. The treatment with $NaNO_2$ converts the hemoglobin within the RBC into methemoglobin, which is paramagnetic, providing the cells with similar magnetic properties of the iRBCs. The tRBCs are suspended in a solution diluted1:6 of healthy RBCs, plasma and PBS. In Fig. 9a, we report the current variation ΔI between the end of a capture phase of 10 minutes and the current after the permanent magnet removal at different tRBCs concentrations. The signal from infected samples (inset in Fig. 9a) follows the expected theoretical behavior shown in Fig. 1. The signal amplitude is correctly proportional to the concentration of tRBC, thus to the parasitemia, as expected from Eq. (4). The LoD obtained is equivalent to a signal of 70 nA corresponding to a parasitemia of 40 tRBCs/µl. The higher LoD compared to [27] is attributed to a different configuration of the permanent magnets and to the lower number of electrodes in the new chip layout that have increased the reliability of the diagnostic test with a detrimental effect on the sensitivity of factor 4. In Fig. 9b, we report a photograph taken with a digital microscope showing how iRBCs were captured only in the region of the micro-concentrators.

C. Single-cell resolution

Currently, the limit of detection is set by the residual drift and slow fluctuations of the current signal and by a spurious signal due to the healthy RBCs. As discussed in Sec. IV-A, the designed electronic platform has a lower noise limit opening the possibility to be operated with a noise level compatible with detecting and counting the single cells captured on the chip surface. In order to demonstrate this capability, we designed a dedicated chip layout with a lower number of sensing points, passing from 91 to 4 for each sensor. The drastic reduction of the total area in contact with the biological sample increases the sensor's resistance and correspondingly reduces the current noise given by random fluctuations of the solution conductivity. On the contrary, the

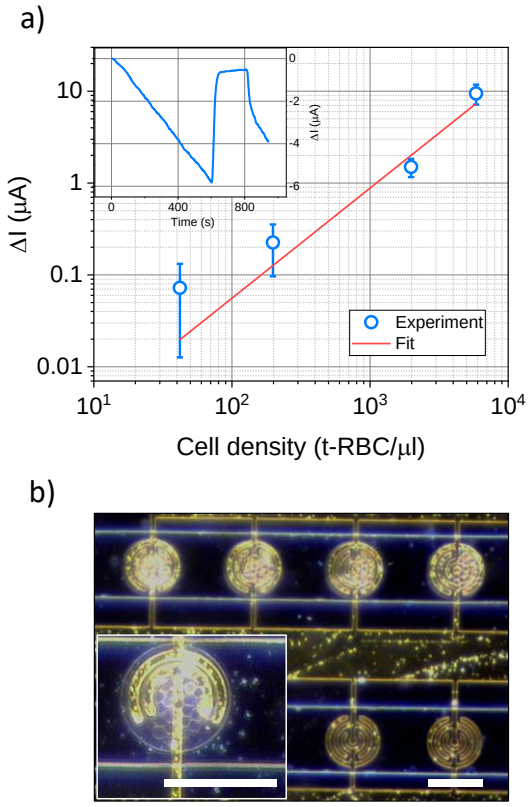

Figure 9 - Calibration curve showing the current variation induced by the RBCs released after capture vs. the cell density (a). Inset in (a) shows a typical signal of a capture (0-600 s) and release (600 s – 800 s) measure. Photograph of the electrodes while capturing RBCs acquired with an optical microscope (b). Inset in (b) is a zoomed photograph of an electrode with a different layout and without healthy RBCs to better show captured cells on it. Scale bars: 40 μm.

current change due to the capture of a single cell is independent of the number of sensing points since they operate in parallel. With these characteristics, the measured noise is reduced to about 3.1 nA rms making the chip suitable for sensing single-cell capture.

In Fig. 10, we report an example of a stepped signal measured with this chip layout. The signal clearly shows each signal step (highlighted by red arrows) corresponding to the capture of individual infected cells, pushing the detection limit to the maximum possible value. Note that operating the platform in this single-cell regime has the additional advantage of reducing the effect of the drift since the current variation due to the capture of a cell happens in a time scale of a few seconds. Moreover, the permanent magnet's release is no longer required, simplifying the experimental setup.

We quantified the single-cell response (SCR) of *P. falciparum* gametocyte–iRBCs, the sexual stages responsible for the human-to-mosquito transmission of the parasite [36], often present also in asymptomatic patients. We measured the steps amplitude of 15 measurements and extracted the signal steps amplitude distribution, reported in Fig. 11a. The kernel probability function (solid yellow line) clearly shows the presence of 3 peaks. We performed a multi-gaussian fit that confirmed the three main contributions (dashed lines). Each peak is centered on a different value and has an amplitude that decreases with the increase of the central value. We

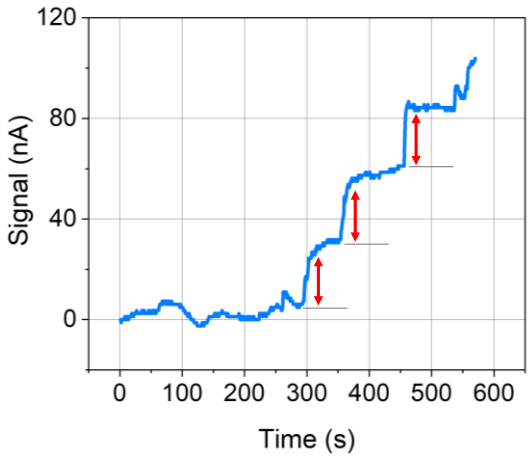

Figure 10 - Single cell signal trace recorded with a solution of P. falciparum gametocytes without healthy RBCs. The jumps (red arrows) are due to the capture of single (discrete) cell.

interpreted the three contributions as the simultaneous capture of one, two, and three cells, respectively. The main peak (dashed red line) is related to the SCR of one gametocyte, which is almost 13±2 nA. The second peak (dashed blue line), centered around 31±2 nA, and the third one (dashed green line), centered around 47±2 nA, represent the double cell response (DCR) and triple cell response (TCR) for gametocytes, which is 2 and 3 cells captured at the same time. This interpretation is supported by the fact that they are multiples of the SCR value. The dispersion of each peak is larger than the noise of the current measurement and can be explained by two phenomena, the variability of the cell size and the orientation of each cell when captured. A cell captured above or close to others can contribute with a slightly different current due to the different perturbation of the electric field and current lines above the sensing electrodes. As discussed in section II, the measured current variation is proportional to the volume of the captured cells. Therefore, thanks to the single-cell sensitivity, we can estimate the volume of a single iRBC. This property of the SCR is intriguing because the parasite changes its volume during its life-cycle so that the single-cell response could provide information on the parasite development stage. In order to verify this possibility, we also tested synchronous asexual blood stage parasites at 18±2 h post RBC invasion, defined as late ring stages. These proliferative asexual stage parasites responsible for malaria pathogenesis represent the alternative developmental pathway with respect to sexual differentiation of the non-dividing gametocytes. The volume of a 18 h ring stage-iRBC is about 1.6 times smaller than the gametocyte-iRBC [37]. In Fig. 11b, we report the distribution of the signal step amplitudes measured with a sample of ring stage parasites. As for gametocytes, three peaks are spotted corresponding to the simultaneous capture of one (centered at 8±2 nA), two (14±2 nA), and three (24±2 nA) cells. Although the data are still preliminary, it is worth noticing that the ratio between the gametocytes and ring stage parasites SCRs is quite close to 1.6, suggesting the possibility of distinguishing the stage of the parasite.

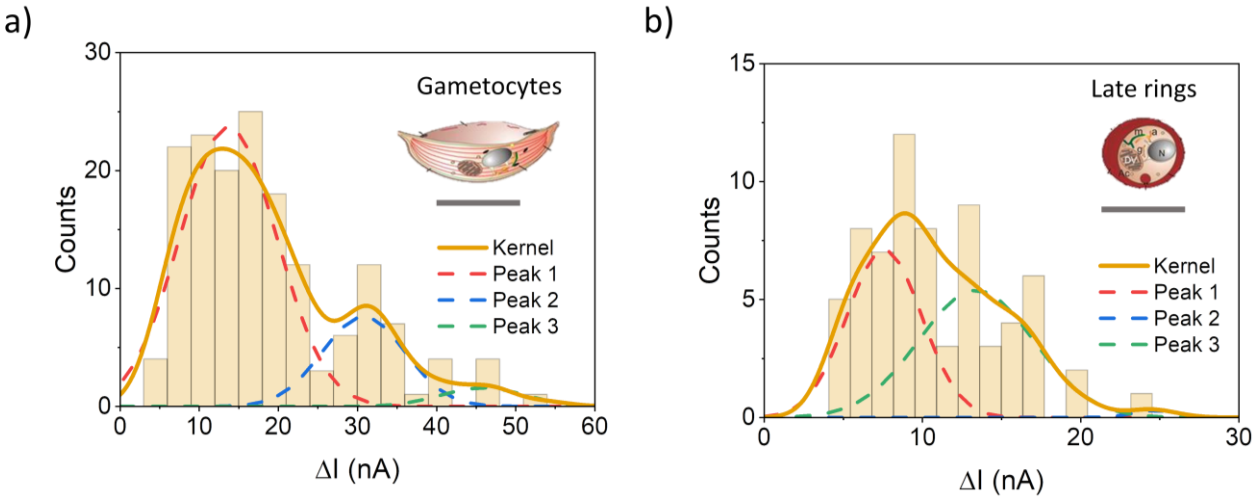

Figure 11 - Distribution of signal steps due to single cells capture for P. falciparum gametocytes (a), cartoon of a gametocyte-infected RBC. For comparison, preliminary results for a suspension of RBCs of which 23% are infected by P. falciparum asexual late ring stage parasites are also reported (b). Kernel distribution is shown (yellow line) with the gaussian components obtained from fit (dashed lines).

The remarkable single-cell sensitivity we demonstrated in the present work implies shifting the technical challenge toward the capability of scanning a high volume of the blood sample while maintaining the limited number of electrodes required to detect a single cell. Future work will explore the addition of a microfluidic system to analyze a large sample volume in a short time, potentially enabling the detection of parasitemia below 1 parasite/µl avoiding expensive techniques such as PCR.

Finally, Table I compares our work with well-established malaria diagnostic tools, such as PCR and RDT, and recently proposed techniques, such as microscopy enhanced by automatic image recognition [38], magneto-optic [20], and photoacoustic [23]. The TMek system discussed in this work offers a good combination of sensitivity and measurement time without requiring complex sample preparation and allowing direct quantification of parasitemia. The readout board achieves single-cell sensitivity without needing high-performance components, making TMek a cost-effective point-of-care device.

V. Conclusions

This work presented the design and the electrical characterization of a low-cost custom electronic board for low-noise signal acquisition from impedimetric biosensors. The board is specifically designed to improve the performance of TMek, a digital lab-on-chip system for rapid and quantitative diagnosis of malaria.

The board consists of a low-cost wideband differential lock-in amplifier and features a multichannel operation and a low noise signal acquisition and digitalization. A DDS generates the counter-phase sinusoidal driving signals used in the differential measurement, while the auto-balancing of the differential sensor is controlled through a microcontroller.

With a 1 kHz - 10 MHz bandwidth, the working frequency can be adjusted according to the experimental requirements.

TABLE I - COMPARISON OF DIFFERENT MALARIA DIAGNOSTIC TOOLS

	PCR [6, 8]	**RDT [6, 8]**	**[38]**	**[20]**	**[23]**	**This work**
Target	DNA of the parasite	Antigens	Parasite	Hemozoin crystals	Infected RBC	Infected RBC
Method	DNA amplification through PCR	lateral flow immunoassay	Microscopy with automatic image recognition	Optical transmission changed by a magnetic field	Photoacoustic effect	Magnetophoretic separation and electrical detection
Sensor	Fluorescence detection	Visual inspection	Microscope coupled to a smartphone	Photodetector	Surface acoustic wave (SAW) sensor	Gold electrodes for impedance measurement
Detection limit	1 p/µl	100 - 200 p/µl	n. a. (40 – 100 p/µl for standard microscopy)	Equivalent to about 50 p/µl	25000 p/µl	40 parasite/µl demonstrated single-cell sensitivity
Test time	45 min	15 min	At least 10 min for Giemsa staining of blood film	1 min + sonication to lyse the RBCs and release the hemozoin	2 min	10 min
Comments	High cost, qualified personnel	Low cost	Medium cost, no portable	No direct assessment of parasitemia	Currently expensive and no portable	Low-cost and portable

The noise of the front-end electronics is demonstrated to be lower than the noise introduced by the sensors.

The system allows the detection of a variation as small as 15 ppm of the sensor impedance at 1 MHz in real conditions. This value is remarkably low, even better than bulky and expensive commercial lock-in amplifiers operating at the same frequency.

Finally, we exploited the performances mentioned above in the acquisition setup of TMek, demonstrating for the first time the single-cell sensitivity in a digital rapid diagnostic test for malaria. This result has the important implication of virtually enabling unprecedented sensitivity in low-cost, on-field detection of this high burden disease.

ACKNOWLEDGMENT

Dr. R. Grande and Prof. S. Antinori from Sacco hospital, Milan, Italy, are thanked for their help and support during the tests on human blood samples. Tecnochimica S.p.a. is thanked for supplying Ni sulfamate solution. This work has been partially carried out at Polifab, the micro and nanofabrication facility of Politecnico di Milano.

REFERENCES

[1] P. Rosenthal, "Hemoglobin catabolism and iron utilization by malaria parasites," *Mol. Biochem. Parasitol.*, vol. 83, no. 2, pp. 131–139, Dec. 1996.

[2] A. Esposito *et al.*, "FRET Imaging of Hemoglobin Concentration in Plasmodium Falciparum-Infected Red Cells," *PLoS One*, vol. 3, no. 11, p. e3780, Nov. 2008.

[3] M. Giacometti *et al.*, "Electrical and magnetic properties of hemozoin nanocrystals," *Appl. Phys. Lett.*, vol. 113, no. 20, p. 203703, Nov. 2018.

[4] World Health Organization, "World Malaria Report," 2021.

[5] J. Nam, H. Huang, H. Lim, C. Lim, and S. Shin, "Magnetic Separation of Malaria-Infected Red Blood Cells in Various Developmental Stages," *Anal. Chem.*, vol. 85, no. 15, pp. 7316–7323, Aug. 2013.

[6] Unitaid, "Malaria Diagnostics Technology and Market Landscape," 2016.

[7] E. Hempelmann, "Hemozoin Biocrystallization in Plasmodium falciparum and the antimalarial activity of crystallization inhibitors," *Parasitol. Res.*, vol. 100, no. 4, pp. 671–676, Jan. 2007.

[8] P. Berzosa *et al.*, "Comparison of three diagnostic methods (microscopy, RDT, and PCR) for the detection of malaria parasites in representative samples from Equatorial Guinea," *Malar. J.*, vol. 17, no. 1, p. 333, Dec. 2018.

[9] A. Mbanefo and N. Kumar, "Evaluation of Malaria Diagnostic Methods as a Key for Successful Control and Elimination Programs," *Trop. Med. Infect. Dis.*, vol. 5, no. 2, p. 102, Jun. 2020.

[10] M. Imwong *et al.*, "High-Throughput Ultrasensitive Molecular Techniques for Quantifying Low-Density Malaria Parasitemias," *J. Clin. Microbiol.*, vol. 52, no. 9, pp. 3303–3309, Sep. 2014.

[11] I. Molina-de la Fuente, A. Pastor, Z. Herrador, A. Benito, and P. Berzosa, "Impact of Plasmodium falciparum pfhrp2 and pfhrp3 gene deletions on malaria control worldwide: a systematic review and meta-analysis," *Malar. J.*, vol. 20, no. 1, p. 276, Dec. 2021.

[12] R. Thomson *et al.*, "pfhrp2 and pfhrp3 Gene Deletions That Affect Malaria Rapid Diagnostic Tests for Plasmodium falciparum: Analysis of Archived Blood Samples From 3 African Countries," *J. Infect. Dis.*, vol. 220, no. 9, pp. 1444–1452, Sep. 2019.

[13] N. Kumar *et al.*, "Genetic deletion of HRP2 and HRP3 in Indian Plasmodium falciparum population and false negative malaria rapid diagnostic test," *Acta Trop.*, vol. 125, no. 1, pp. 119–121, Jan. 2013.

[14] E. Y. Lukianova-Hleb *et al.*, "Hemozoin-generated vapor nanobubbles for transdermal reagent- and needle-free detection of malaria," *Proc. Natl. Acad. Sci.*, vol. 111, no. 3, pp. 900–905, Jan. 2014.

[15] O. Rifaie-Graham *et al.*, "Hemozoin-catalyzed precipitation polymerization as an assay for malaria diagnosis," *Nat. Commun.*, vol. 10, no. 1, p. 1369, Dec. 2019.

[16] "MACS® Cell Separation, Miltenyi Biotec.".

[17] C. Ribaut *et al.*, "Concentration and purification by magnetic separation of the erythrocytic stages of all human Plasmodium species," *Malar. J.*, vol. 7, no. 1, p. 45, Dec. 2008.

[18] K.-H. Han and A. B. Frazier, "Paramagnetic capture mode magnetophoretic microseparator for high efficiency blood cell separations," *Lab Chip*, vol. 6, no. 2, pp. 265–273, 2006.

[19] A. Blue Martin, W.-T. Wu, M. V. Kameneva, and J. F. Antaki, "Development of a High-Throughput Magnetic Separation Device for Malaria-Infected Erythrocytes," *Ann. Biomed. Eng.*, vol. 45, no. 12, pp. 2888–2898, Dec. 2017.

[20] R. Kumar, A. K. Verma, S. Shrivas, P. Thota, M. P. Singh, S. Rajasubramaniam, A. Das, and P. K. Bharti, "First successful field evaluation of new, one-minute haemozoin-based malaria diagnostic device," *EClinicalMedicine*, vol. 22, p. 100347, May 2020.

[21] S. E. McBirney, D. Chen, A. Scholtz, H. Ameri, and A. M. Armani, "Rapid Diagnostic for Point-of-Care Malaria Screening," *ACS Sensors*, vol. 3, no. 7, pp. 1264–1270, Jul. 2018.

[22] S. Wang, C. Yang, P. Preiser, and Y. Zheng, "A Photoacoustic-Surface-Acoustic-Wave Sensor for Ring-Stage Malaria Parasite Detection," *IEEE Trans. Circuits Syst. II Express Briefs*, vol. 67, no. 5, pp. 881–885, May 2020.

[23] W. Wang, Z. Zheng, C. Yang, Z. Fang, S. Wang, C. Yuen, K. Tang, Q. Liu, P. Preiser, and Y. Zheng, "Laser-Induced Surface Acoustic Wave Sensing-Based Malaria Parasite Detection and Analysis," *IEEE Trans. Instrum. Meas.*, vol. 71, pp. 1–9, 2022.

[24] A. P. Hole and V. Pulijala, "An Inductive-Based Sensitive and Reusable Sensor for the Detection of Malaria," *IEEE Sens. J.*, vol. 21, no. 2, pp. 1609–1615, Jan. 2021.

[25] S. O. Catarino, P. Felix, P. J. Sousa, V. Pinto, M. I. Veiga, and G. Minas, "Portable Device for Optical Quantification of Hemozoin in Diluted Blood Samples," *IEEE Trans. Biomed. Eng.*, vol. 67, no. 2, pp. 365–371, Feb. 2020.

[26] V. Baptista, W. K. Peng, G. Minas, M. I. Veiga, and S. O. Catarino, "Review of Microdevices for Hemozoin-Based Malaria Detection," *Biosensors*, vol. 12, no. 2, p. 110, Feb. 2022.

[27] M. Giacometti *et al.*, "A Lab-On-chip Tool for Rapid, Quantitative, and Stage-selective Diagnosis of Malaria," *Adv. Sci.*, vol. 8, no. 14, p. 2004101, Jul. 2021.

[28] F. Milesi, M. Giacometti, L. P. Coppadoro, G. Ferrari, G. B. Fiore, and R. Bertacco, "On-Chip Selective Capture and Detection of Magnetic Fingerprints of Malaria," *Sensors*, vol. 20, no. 17, p. 4972, Sep. 2020.

[29] S. Gawad, L. Schild, and P. Renaud, "Micromachined impedance spectroscopy flow cytometer for cell analysis and particle sizing," *Lab Chip*, vol. 1, no. 1, p. 76, 2001.

[30] T. Sun and H. Morgan, "Single-cell microfluidic impedance cytometry: a review," *Microfluid. Nanofluidics*, vol. 8, no. 4, pp. 423–443, Apr. 2010.

[31] G. Gervasoni, M. Carminati, and G. Ferrari, "Switched ratiometric lock-in amplifier enabling sub-ppm measurements in a wide frequency range," *Rev. Sci. Instrum.*, vol. 88, no. 10, p. 104704, Oct. 2017.

[32] M. Carminati, G. Gervasoni, M. Sampietro, and G. Ferrari, "Note: Differential configurations for the mitigation of slow fluctuations limiting the resolution of digital lock-in amplifiers," *Rev. Sci. Instrum.*, vol. 87, no. 2, p. 026102, Feb. 2016.

[33] M. Giacometti, *et al.*, "On-chip magnetophoretic capture in a model of malaria-infected red blood cells," *Biotechnol. Bioeng.*, vol. 119, no. 4, pp. 1129–1141, Apr. 2022.

[34] C. Lambros and J. P. Vanderberg, "Synchronization of Plasmodium falciparum Erythrocytic Stages in Culture," *J. Parasitol.*, vol. 65, no. 3, p. 418, Jun. 1979.

[35] J. J. Barron and C. Ashton, "The effect of temperature on conductivity measurement," *TSP*, vol. 7, no. 3, pp. 1–5, 2005.

[36] R. Tuteja, "Malaria − an overview," *FEBS J.*, vol. 274, no. 18, pp. 4670–4679, Sep. 2007.

[37] M. K. Dearnley *et al.*, "Origin, composition, organization and function of the inner membrane complex of Plasmodium falciparum gametocytes," *J. Cell Sci.*, Jan. 2012.

[38] F. Yang, *et al.*, "Deep Learning for Smartphone-Based Malaria Parasite Detection in Thick Blood Smears," *IEEE J. Biomed. Heal. Informatics*, vol. 24, no. 5, pp. 1427–1438, May 2020.